Geochemistry Geophysics Geosystems G3
AN ELECTRONIC JOURNAL OF THE EARTH SCIENCES
Published by AGU and the Geochemical Society

Data Brief
Volume 9, Number 12
5 December 2008
Q12009, doi:10.1029/2008GC002204
ISSN: 1525-2027

Globally aligned photomosaic of the Lucky Strike hydrothermal vent field (Mid-Atlantic Ridge, 37°18.5′N): Release of georeferenced data, mosaic construction, and viewing software

J. Escartín
Groupe de Géosciences Marines, IPGP, CNRS, Case 89, 4 Place Jussieu, F-75252 Paris, France (escartin@ipgp.jussieu.fr)

R. García, O. Delaunoy, J. Ferrer, N. Gracias, A. Elibol, X. Cufi, and L. Neumann
Computer Vision and Robotics Group, Department of Electronics, Informatics and Automation, University of Girona, Campus Montilivi, E-17071 Girona, Spain

D. J. Fornari and S. E. Humphris
Department of Geology and Geophysics, Woods Hole Oceanographic Institution, Woods Hole, Massachusetts 02543, USA

J. Renard
COGIT, Institut Géographique National, F-94165 Saint Mandé, France

[1] We present a georeferenced photomosaic of the Lucky Strike hydrothermal vent field (Mid-Atlantic Ridge, 37°18′N). The photomosaic was generated from digital photographs acquired using the ARGO II seafloor imaging system during the 1996 LUSTRE cruise, which surveyed a ~1 km^2 zone and provided a coverage of ~20% of the seafloor. The photomosaic has a pixel resolution of 15 mm and encloses the areas with known active hydrothermal venting. The final mosaic is generated after an optimization that includes the automatic detection of the same benthic features across different images (feature-matching), followed by a global alignment of images based on the vehicle navigation. We also provide software to construct mosaics from large sets of images for which georeferencing information exists (location, attitude, and altitude per image), to visualize them, and to extract data. Georeferencing information can be provided by the raw navigation data (collected during the survey) or result from the optimization obtained from image matching. Mosaics based solely on navigation can be readily generated by any user but the optimization and global alignment of the mosaic requires a case-by-case approach for which no universally software is available. The Lucky Strike photomosaics (optimized and navigated-only) are publicly available through the Marine Geoscience Data System (MGDS, http://www.marine-geo.org). The mosaic-generating and viewing software is available through the Computer Vision and Robotics Group Web page at the University of Girona (http://eia.udg.es/~rafa/mosaicviewer.html).

Components: 8790 words, 10 figures, 1 table.

Keywords: mid-ocean ridge; photomosaic; MoMAR; Lucky Strike; hydrothermal field.

Index Terms: 3035 Marine Geology and Geophysics: Midocean ridge processes; 0450 Biogeosciences: Hydrothermal systems (1034, 3017, 3616, 4832, 8135, 8424); 0540 Computational Geophysics: Image processing.

Received 2 September 2008; **Revised** 24 September 2008; **Accepted** 3 October 2008; **Published** 5 December 2008.

Escartín, J., et al. (2008), Globally aligned photomosaic of the Lucky Strike hydrothermal vent field (Mid-Atlantic Ridge, 37°18.5′N): Release of georeferenced data, mosaic construction, and viewing software, *Geochem. Geophys. Geosyst.*, *9*, Q12009, doi:10.1029/2008GC002204.

1. Introduction

[2] Seafloor imagery is routinely acquired during near-bottom mapping surveys conducted with submersibles, remotely operated vehicles (ROVs) and autonomous underwater vehicles (AUVs) [e.g., *Ballard et al.*, 2002; *Humphris et al.*, 2002; *Soule et al.*, 2005; *Eustice et al.*, 2006; *German et al.*, 2006]. Deep-sea hydrothermal fields have long been the targets of such studies, where imagery is necessary to both characterize the nature and distribution of geological features and biological communities, and to document the temporal variations associated with the active processes operating at these sites. Deep-sea imaging studies often yield large numbers of images (100s to 1000s) that are frequently underutilized largely because of the difficulties inherent in visualizing large data sets where navigation and vehicle attitude errors and uncertainty complicate processing multiple images [*Rzhanov et al.*, 2003; *Singh et al.*, 2007; *Yoerger et al.*, 2007].

[3] The Lucky Strike hydrothermal field is located on the summit of a central volcano, near the middle of the Lucky Strike segment (∼1600 m depth) [*Langmuir et al.*, 1997], along the Mid-Atlantic Ridge (MAR) axis at ∼37°18′N (Figure 1). The seamount is underlain by an axial magma chamber (AMC) at midcrustal level (∼3 km) that extends beneath the rift valley for ∼8 km along-axis and is <6 km wide [*Singh et al.*, 2006]. The AMC is likely to be the heat source controlling the hydrothermal circulation. The hydrothermal vents are located primarily along the slopes, which correspond to fault scarps flanking an axial graben [*Escartín et al.*, 2005; *Ondreas et al.*, 2008], and surround the lava lake in the center of the summit area. This zone encompasses numerous active black smokers with outflow temperatures of >300°C and zones of lower temperature diffuse flow (<100°C), in addition to inactive vents [*Fouquet et al.*, 1994; *Langmuir et al.*, 1997; *Humphris et al.*, 2002; *Ondreas et al.*, 2008]. The hydrothermal activity at this field appears to have at least two distinct geochemical sources [*Von Damm et al.*, 1998; *Charlou et al.*, 2000], which separately feed the vents located in the northwestern and eastern portions of the field.

[4] Extensive seafloor imagery of this site was acquired during the LUSTRE cruise in 1996 and particularly over the actively venting areas [*Scheirer et al.*, 2000; *Humphris et al.*, 2002] (Figure 2). In this paper we present three georeferenced photomosaics of the hydrothermal field derived from LUSTRE'96 images, with a pixel resolution of 15 mm and an overall coverage of ∼20% of the surveyed area. The first and second photomosaics are derived from individual image frames that are rotated, scaled, and placed in a geographic reference frame using navigation and attitude information derived from the ARGO II vehicle used during the survey. The third photomosaic was generated after image registration and optimization, to obtain a global alignment of images, and constrained with the original navigation to avoid spatial drift of the imagery.

[5] Several available software tools can be used to display georeferenced images. However, these tools are inadequate for the visualization of large areas at the resolution required for seafloor studies or to extract relevant information for scientific purposes. We have thus developed software to automatically generate georeferenced mosaics using the vehicle navigation information, to visualize, extract data and information (e.g., plotting, digitization, georeferenced image extraction), and which can be used to compare mosaics of the same area collected at different times for temporal studies. A set of Matlab™ tools provided use standard navigation data and image file information to generate a GMML (General Mosaic Markup Language) file with the information necessary to create the georeferenced mosaic. This file, together with the original greyscale or color imagery, is used by the *MosaicViewer* software to construct the mosaic, visualize it, and extract information. Photomosaics created from raw navigation data alone (i.e., scaling, rotating, and positioning of images) can be created readily and are adequate for most scientific purposes, as the resulting images are geographically registered, oriented, and scaled. Further processing is required to generate an optimized mosaic. This requires specialized software to carry out

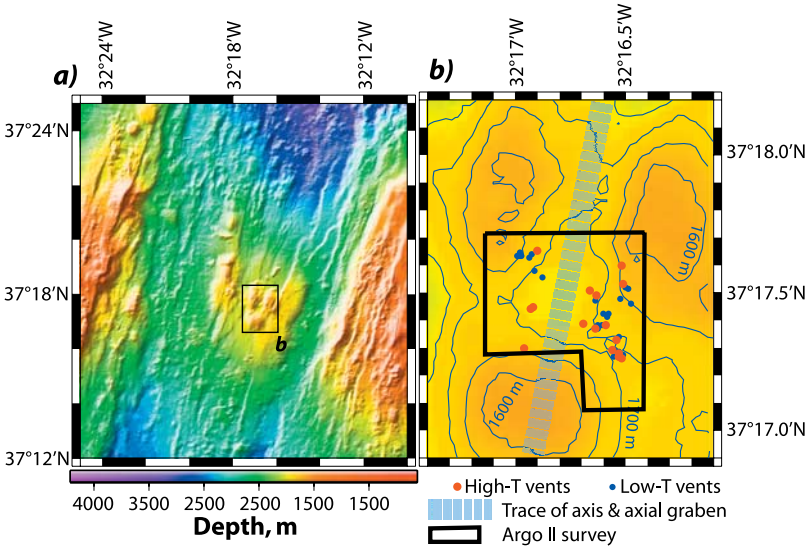

Figure 1. (a) Multibeam bathymetry of the Lucky Strike segment center, showing the faulted central volcano within the axial valley. Data from the SISMOMAR, FLORES, and SUDAÇORES cruises (France). The box corresponds to Figure 1b. (b) Summit of the central volcano showing three local highs surrounding a local low within the axial graben. High- and low-temperature vents (>300°C and <100°C, respectively) surround this low and concentrate along the walls of the axial graben. Blue 50-m contours correspond to the multibeam bathymetry (Figure 1a), and the 10 m contours correspond to a bathymetry map derived from ARGO II depth and altitude soundings [*Scheirer et al.*, 2000; *Humphris et al.*, 2002] along survey tracks (see Figure 2). Bathymetry is illuminated from the west.

feature matching across images and their relocation and cannot be made available as a standard package for general use.

2. Data Acquisition, Vehicle Navigation, and Vehicle Attitude

[6] Accurate navigation data (position, altitude, heading, pitch and roll) are necessary to generate mosaics with the software presented here. Present-day surveys benefit from high-quality navigation data which is routinely acquired by deep submergence vehicles, and that includes north-seeing fiber optic gyros, Doppler velocity log (DVL), acoustic location, or inertial navigation. To construct mosaics these data require corrections to account for the position of the camera with respect to the navigation sensors (i.e., altimeter and transponder). This contrasts with legacy data, which owing to technological limitations at the time, may require correction and preprocessing specific to each survey so as to obtain usable navigation data, as in the case of the LUSTRE'96 ARGO II survey of Lucky Strike presented here.

[7] The ARGO II system [*Bowen et al.*, 1993; *Bachmayer et al.*, 1998; *Scheirer et al.*, 2000] used during the LUSTRE'96 cruise was equipped with an electronic still CCD camera, a 675 kHz altim-

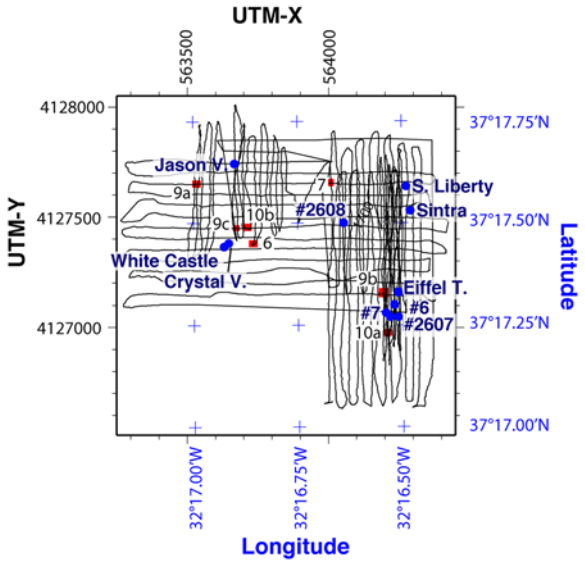

Figure 2. ARGO II tracks over the Lucky Strike hydrothermal field. Relief in the area reaches >100 m (10-m contours, derived from ARGO II depth and altimetry [*Scheirer et al.*, 2000]). The main high-temperature vents are also indicated. UTM coordinates and reference system correspond to the transponder navigation deployed for the LUSTRE'96 cruise. Red boxes and associated numbering correspond to the location of panels in Figures 9 and 10.

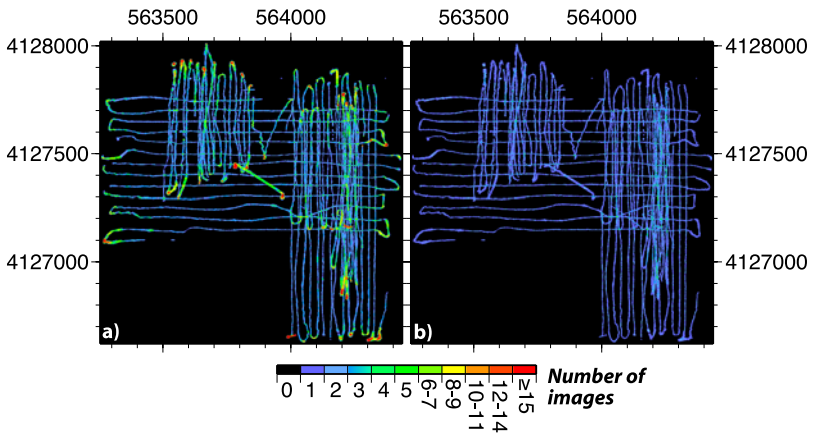

Figure 3. Map of the study area showing the overall image coverage and the number of images over a given area (see tracks in Figure 2). (a) The mosaic containing all the images shows areas with considerable image overlap near some of the vents and at turns. (b) Image repetition is considerably reduced if consecutive images with ≤5% overlap are retained. Two photomosaics are built with all the images in Figure 3a and the subset shown in Figure 3b (see text for details).

eter, inclinometers for pitch and roll, and a fluxgate compass for the heading. The vehicle was navigated using a bottom-moored transponder long baseline (LBL) network. Vehicle locations at acoustic fixes are estimated to have an error of less than 10 m, as confirmed by the identification of the same benthic features in images of crossing tracks acquired at different times during the cruise. ARGO II was towed at 3–15 m (~10.2 ± 2.5 m in average) above the seafloor at speeds of ~0.25–0.5 kt. North-south tracks had variable spacing between ~25 and <10 m, while east-west tracks had an average spacing of ~50 m (Figure 2). A total of 20,823 images were acquired every 13 s during the 92-h survey, with an average along-track spacing of ~3 m. The images where acquired with a Marquest ESC9100 camera equipped with a 576 × 384 imaging chip and a 28 mm lens. This configuration provides a 45° × 31° field of view, covering 41.5 m^2 of seafloor at an altitude of 10 m, with a pixel resolution of ~15 mm. Images have been individually equalized to correct for uneven illumination using a contrast limited adaptive histogram equalization (CLAHE) [*Zuiderveld*, 1994]; the original images are not available and the equalization parameters are not known.

[8] The position of the camera is obtained from the UTM coordinates of the vehicle and from the 17 cm shift in the X direction (reference frame of the ARGO II vehicle) between the camera and the LBL acoustic receiver. For this survey the camera was located at the same Z position as the altimeter. The camera location (UTM coordinates), and altitude of the vehicle above the seafloor were then used to place and scale the images in a georeferenced photomosaic (Figure 3). These data provide seafloor imagery for ~20% of the surveyed area, varying locally from <10% over the lava pond at the center of the survey area, and reaching a maximum of ~75% over some of the actively venting areas on the NW and east slopes flanking the lava pond (Figure 3a).

[9] The attitude of the vehicle, and particularly the heading, is a critical parameter for the correct projection of images in a georeferenced coordinate system (Figure 4). Pitch and roll of ARGO II during this survey were close to zero and show negligible variations (0.6 ± 0.1° and 1.2 ± 0.1°, respectively). Consequently, for this survey we assumed that the images were acquired vertically, although the software accounts for oblique images if accurate attitude data were available. We used the vehicle altitude to determine image scaling for their projection onto a flat bottom.

[10] ARGO II was equipped with a compass to record heading, but this information was discarded due to significant drift of the fluxgate compass and random resets of the compass during the survey. Furthermore, examination of the imagery shows that the vehicle was oriented subperpendicular (100°) to the towing direction. To obtain a usable estimate of the heading, we relied instead on the alignment of consecutive images and the transponder navigation to confirm the overall direction of travel and orientation for the system. Matching features between successive images allows an accurate estimate of the relative motion between

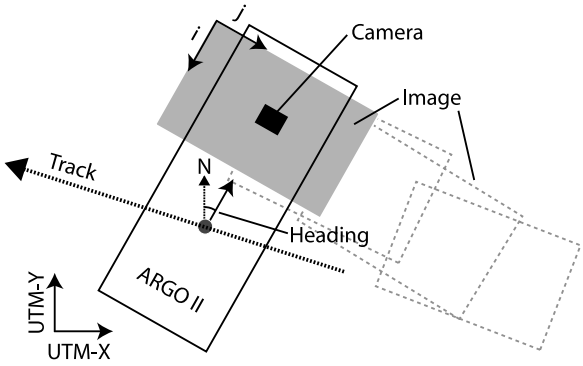

Figure 4. Diagram of the geometry of ARGO II system and orientation of images with respect to the towing direction (track). Dashed boxes correspond to previously acquired images.

consecutive frames. This motion is computed by means of a planar transformation (i.e., homography, as per *Negahdaripour et al.* [2005]) between consecutive images, and permits 2-D translation, rotation and scaling of the images. The path between two nonconsecutive images is calculated by multiplying the incremental homographies of the consecutive images between them.

[11] The homography-derived trajectories were computed for sets of 10 consecutive images throughout the survey area, using the transponder navigation to fix the position of the first image in each set, as shown in Figure 5a. The partial trajectories show a curved path due to the error propagation in the multiplication of incremental homographies. These errors may arise from a slightly tilt of the vehicle or the camera, instead of the zero pitch and roll assumed, or from the three-dimensional nature of the seafloor instead of the assumed flat bottom. The overall orientation of the first portion of the 10-image partial trajectory has the least accumulated error, and for most of the survey is in good agreement with the visually determined ~100° orientation. We have identified areas in which the homographies show a 180° rotation with respect to this assumed orientation, which correspond to an apparent rotation of the vehicle heading with respect to the track orientation (compare northward and southward tracks in Figure 5a). The apparent orientation flips are caused by the vehicle maintaining its absolute orientation during a turn instead of following its track. Owing to these changes in vehicle heading, and to the lack of reliable gyro data, we recalculated the vehicle heading for the whole survey with homography-derived trajectories by (1) rotating each set of images so as to match the average orientation given by the first three images in each set with the orientation of the track at the location of the first image and (2) by assigning the new heading to all the images in the set and thus generating a new heading record for the whole survey. For the most part, corrections are small (<20°), and are close to 180° for areas where ARGO II rotated with respect to the track (see northward and southward tracks in Figure 3b, respectively).

3. Generation of the Photomosaics

3.1. Navigation-Based Photomosaics

[12] To construct a seafloor mosaic based on vehicle navigation, we have developed software that determines the scaling and orientation of each image from the heading and altitude of the vehicle, and places them based on the camera position, as provided by the navigation file (Figure 4). If available, the program can also use the optical characteristics of the camera in the form of the

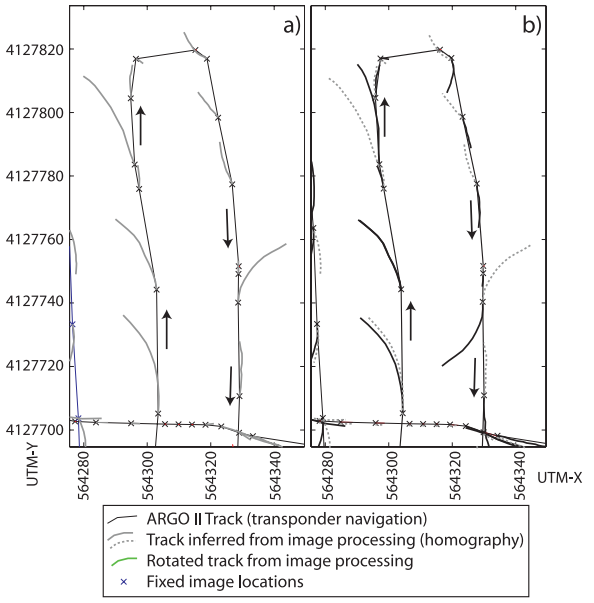

Figure 5. (a) ARGO II tracks and towing direction (arrows), and partial trajectories calculated from sets of 10 pictures (gray curves), and the assumed ~100° ARGO II orientation with respect to the track. Note that ARGO II shows a ~180° change in direction with respect to the track at the turn between northward and the southward tracks. (b) The rotation required to minimize the difference between the track direction and that of the initial portion of the trajectory (black bold lines) provides an estimate of the vehicle's heading. This rotation also corrects the apparent ~180° rotation of the vehicle with respect to the track direction.

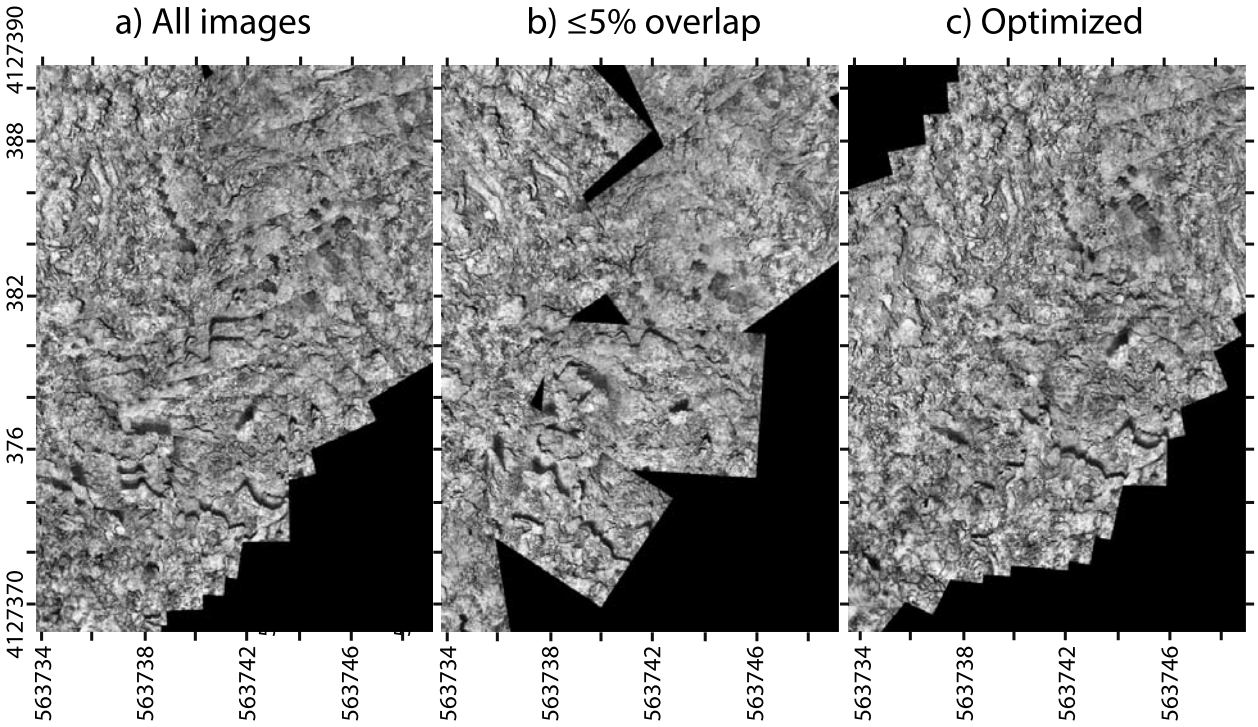

Figure 6. Comparison of three mosaics from an area of the Lucky Strike Field. (a) The mosaic including all images shows areas with overlapping frames that hinder the visualization of the terrain. (b) The mosaic with a reduced number of photos allows a clear view of individual frames and therefore of seafloor textures and structures, although with reduced coverage. (c) The optimized mosaic shows continuous imagery across frames, after correction of the navigation and reprojection of images.

intrinsic parameters matrix [*Bouguet and Perona*, 1998], commonly used in the computer vision community (see Appendix A). Additionally, the user can set the desired pixel size of the final mosaic based on the survey characteristics, area covered by individual images, and the image resolution. At Lucky Strike the use of all images (20,823, Figure 3a) provides the most extensive coverage of the study area (~290,000 m^2), but the large overlap of some images (Figures 6a and 6b) results both in the masking of features by consecutive frames, and the repetition of misaligned edges, which hinder visualization of seafloor structures. We have generated a second mosaic with a subset of the images (11,602). For this mosaic we included only the images that showed a maximum overlap of 5% with previous images (Figure 3b). While this mosaic results in a slightly reduced coverage (~262,000 m^2), individual images are often fully visible and seafloor features more clearly shown (Figure 6).

[13] Errors in the scaling, rotation, and location of images based on the navigation and inferred vehicle attitude result in inconsistencies across consecutive and nonconsecutive frames, either along or across tracks (Figure 7). Misalignment of features between consecutive frames is relatively small (typically <1–2 m, Figure 7) and arises from errors in the heading, pitch and roll, and from seafloor topography. This error increases to 6 ± 4 m for a total of 78 seafloor features identified near track crossing (e.g., Figure 7) or along adjacent parallel tracks, with a maximum identified offset of 34 m. The average error is lower than but consistent with the nominal ~10–20 m accuracy reported for the ARGO II acoustic transponder navigation [*Scheirer et al.*, 2000].

3.2. Optimized Photomosaic

[14] Building a large globally aligned photomosaic requires the detection of corresponding points in consecutive images, the prediction of overlaps between nonconsecutive images, and the detection of corresponding points in nonconsecutive images (loop detection). While image processing produces coherent image alignment, it requires position estimates from vehicle navigation to avoid important drifts in the localization of images. All image pairs where correspondence points were found are verified and rejected if the matching is not reliable

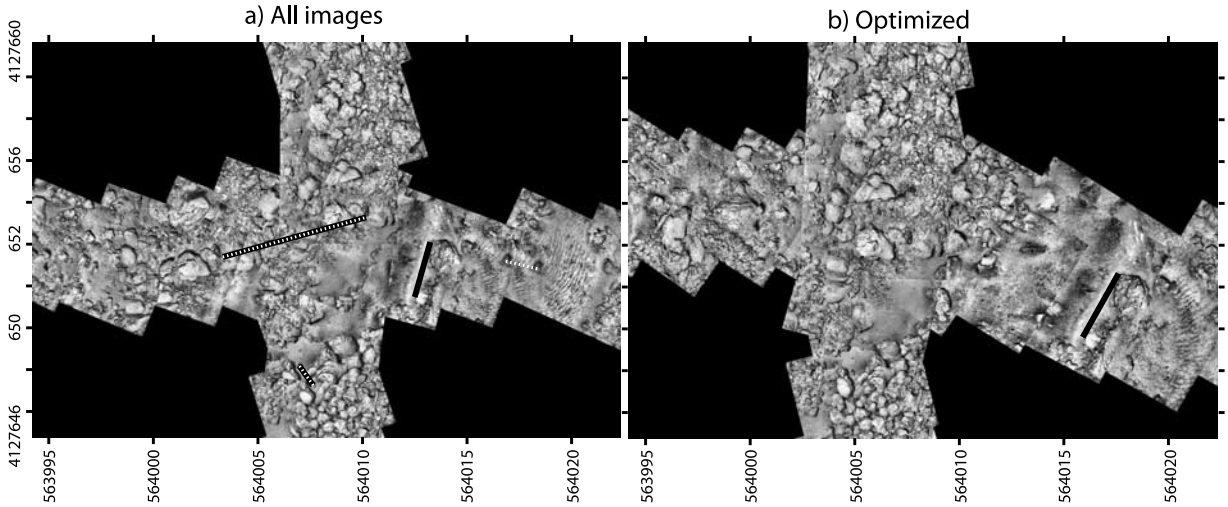

Figure 7. Along- and across-track errors in positioning, scaling and rotation of images in the (a) navigated and (b) optimized mosaics. Dashed lines indicate the same feature in different frames, and the solid black line shows both rotation and scaling differences across tracks. Errors in locations along-track are typically <2 m, while those across track are <10 m (dashed lines).

[*Ferrer et al.*, 2007]. Subsequently, a large nonlinear optimization problem is solved to optimally combine image registration information (matching image pairs) and vehicle navigation data. This optimization generates and improved estimate of the three-dimensional position and orientation of every image and hence of the vehicle.

3.2.1. Registration of Consecutive Images

[15] A crucial part in the mosaicing workflow is the registration of two or more images of the same scene taken at different times and from different viewpoints, to geometrically align them [e.g., *Zitová and Flusser*, 2003]. Some registration methods rely on the detection of salient features using different detectors (e.g., Harris [*Harris and Stephens*, 1988], Hessian [*Beaudet*, 1978], or Laplacian [*Lindeberg*, 1998] detectors), and the computation of a correlation measure for each assumed or possible transformation of the image. More recently, Scale Invariant Feature Transform (SIFT) algorithms [*Lowe*, 2004] have greatly sped up the development salient point detectors and descriptors. The SIFT and subsequent algorithms (e.g., SURF [*Bay et al.*, 2006]) show greater invariance to image scaling, rotation, change in illumination, and 3-D structure. For the LUSTRE′96 mosaic we have followed the SURF method to detect corresponding points in all the pairs of consecutive images, by (1) the use of a Hessian detector to identify individual features, (2) a feature description exploiting gradient information at particular orientations and spatial frequencies [*Mikolajczyk et al.*, 2005], and (3) a matching based on the Euclidean distance between descriptors. Initial matching may produce incorrect correspondences or outliers, which are rejected using a robust estimation algorithm (e.g., RANSAC [*Fischler and Bolles*, 1981]). The remaining inliers are then used to compute the homography that registers both images.

3.2.2. Registration of Nonconsecutive Images

[16] In order to obtain a globally coherent mosaic, the next step is the detection of nonconsecutive overlapping images. When the trajectory of the vehicle crosses over itself, the same area of the seafloor is imaged, providing new constraints for the global alignment of the photomosaic. Possible crossings are identified using available navigation data, and a sequence of images closer than a certain threshold from this point are analyzed to identify candidate image pairs which are then robustly matched using a three-step procedure: (1) SURF features are extracted from both images and matched using RANSAC under a planar projective motion model [*Vincent and Laganière*, 2001; *Brown and Lowe*, 2003]. (2) If enough matched pairs of points are found, then the resulting homography is checked for consistency (proper rotations [*Triggs* 1998]) and for acceptable minimum overlap. (3) For pairs that have been retained after verifications outlined in step 2, we search for further

correspondences. The image pairs are then aligned according to the previously estimated homography. Next, we extract Harris corners [*Harris and Stephens*, 1988] in one of the images, and their correspondences are detected through correlation [*Garcia et al.*, 2003] in the other image. If an insufficient number of correspondences are found, the image pair is rejected. Moreover, the image pair is also rejected if their overlapping area is smaller than a predefined threshold (e.g., 10%). All thresholds and parameters used in the procedure described above depend on specific survey and mosaic configurations, and thus are manually tuned. The pairs retained with the associated correspondence points are used as an input for the global alignment, as described in section 3.2.3.

3.2.3. Global Alignment

[17] Small errors that occur during image registration cause misalignment when images are mapped on a mosaic (global) frame, and require a global alignment calculated from successive motion parameters between images consecutive in time. This procedure requires global alignment methods [*Sawhney et al.*, 1998; *Marzotto et al.*, 2004] based on a minimization of distances between correspondences.

[18] For the LUSTRE'96 survey, we first estimate the pose (position and orientation) of the camera when the image was acquired for each image in the sequence. The subsequent optimization estimates the three-dimensional camera poses. The camera trajectory is parameterized using 6 degrees of freedom (three-dimensional position and orientation, while each camera pose is parameterized with seven variables (X, Y, Z, and a unitary quaternion to describe camera rotation in three dimensions [*Salamin*, 1979]). The initial trajectory used in the optimization is that obtained from the navigation data, and the nonlinear optimization procedure (bundle adjustment) will minimize a cost function [*Ferrer et al.*, 2007] defined as a stack of residuals coming from four different sources, which are weighed according to sensor uncertainties:

[19] 1. The first is point correspondences. For each overlapping pair computed in the previous section, a planar transformation and a set of correspondences was stored, which are used as input constraints to the bundle adjustment optimization.

[20] 2. The second is fiducial point readings. For certain surveying and monitoring applications, a number of landmarks with known x and y coordinates (fiducial points) may be available and can be added as constraints.

[21] 3. The third is LBL positions. Each acoustic LBL position generates three residuals (over the x, y, and z directions). In the LUSTRE'96 data set, one image was acquired every 13 s, and only LBL readings synchronous with an image acquisition are taken into account.

[22] 4. The fourth is angular camera readings. Navigation data commonly provides roll, pitch, and heading orientation of the vehicle, which are transformed to 3-D camera rotations. For each camera pose we compute the residuals for roll, pitch, and yaw.

3.2.4. Crossover Detection and Optimization Iteration

[23] We improve mosaic alignment through several iterations of crossover detection and optimization. After each iteration, the resulting optimized trajectory of the camera is transformed to navigation data, which in turn is used as starting point for a new algorithm iteration and bundle adjustment to find new constraints (i.e., more overlapping image pairs near crossings). Iterations are repeated until no new crossovers are detected.

[24] The minimization of the cost function is achieved in a nonlinear least squares manner, and requires the computation of a Jacobian matrix that includes the derivatives of all residuals with respect to the camera trajectory parameters. As each residual depends on a reduced number of parameters, the matrix is both sparse and shows a constant sparsity pattern allowing an efficient computation of the Jacobian. In our implementation, analytic expressions were derived and used for computing the blocks of the Jacobian matrix [*Triggs et al.*, 2000].

[25] The final globally aligned LUSTRE'96 mosaic of the Lucky Strike area is generated from the optimization of a nonlinear equation system with 141,582 parameters to be estimated (seven per image) and 459,216 residuals for point and match correspondences over 28,701 image pairs, in addition to 60,678 angular residuals (three readings over 20,226 images). Finally, 1788 residuals were obtained from 596 images with absolute LBL positions. Solving such a large nonlinear system required specialized optimization software (*Xpress* library by DashOptimization).

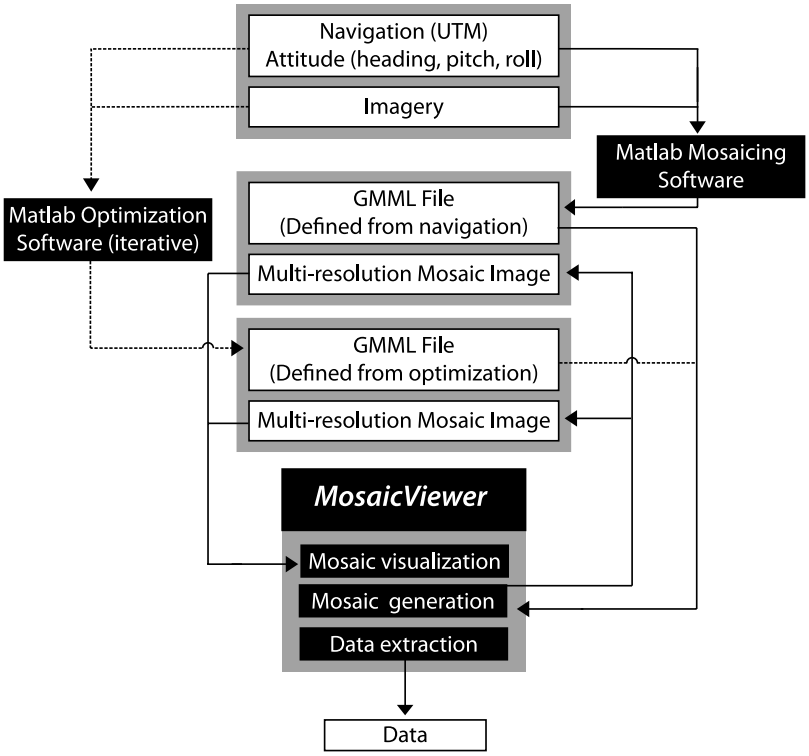

Figure 8. Flow diagram to generate navigation based and globally optimized photomosaics. Navigation based mosaics can be generated by any user based on a navigation file for the camera based on vehicle navigation and the associated imagery (solid lines). These data are used to generate a GMML file (see text) that is the blueprint to generate the mosaic with *MosaicViewer*. The flow indicated by solid lines with arrows can be recreated by any user with the software provided in this paper. The globally optimized mosaic requires specialized software and processing adapted for each survey (see text). The resulting mosaics can be visualized and exploited scientifically by the software provided.

3.3. Processing and Viewing of Photomosaics

[26] We provide the software developed by the Computer Vision and Robotics Group (University of Girona, Spain) used to construct the Lucky Strike mosaics. This software, released together with the mosaics, can generate mosaics from navigation data and be a valuable to study areas for which imagery and appropriate vehicle navigation exists. Details of file formats and a more technical description of the software and files are provided in Appendix A, and a summary of the workflow and different processing and software components in Figure 8. The user must generate the required navigation files corrected for the camera position, and including survey-specific corrections. The navigation file, formatted as described in Appendix A, is used by a Matlab™ function to generate a file containing the attitude (3-D position and orientation) of the camera, and the absolute homographies (2-D position, orientation, and scale) of each image in the mosaic coordinate system. This file, which is generated in GMML metalanguage (General Mosaic Markup Language, see Appendix A) is a blueprint loaded and used by *MosaicViewer* to construct the mosaic. *MosaicViewer* is compiled for Windows XP and Vista, Linux, and a Mac OS X version is under development. This software automatically generates a set of images at different resolutions that are then accessed to visualize the mosaic, to import data, and to digitize information. This software is not usable as a geographic information system or as a map-generation program; for these purposes, data should be exported and processed with adequate software. In addition to the *MosaicViewer* files, we have generated an ArcCiew GIS layer of the optimized LUSTRE'96 mosaic, which is available for download at the MGDS site.

3.4. Data and Software Release Information

[27] The complete (20,823 images) and the partial Lucky Strike navigated mosaics (11,602 images), the optimized mosaic (~1.5 Gb each), the corresponding GIS layer (~7 Gb) and the original digital photos

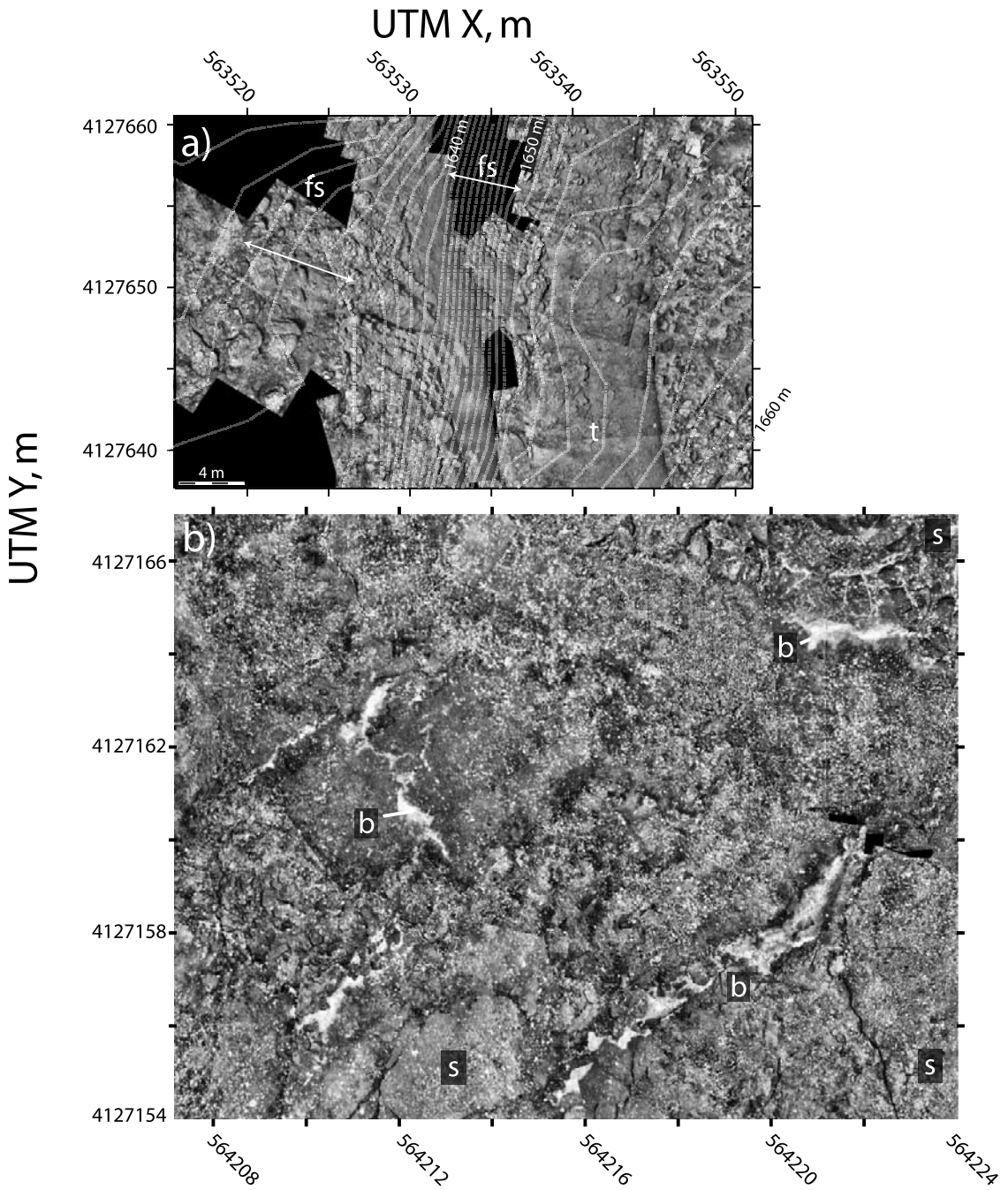

Figure 9. Details of the Lucky Strike optimized mosaic. (a) Fault scarp (arrows) and associated talus in the northwestern part of the survey area. (b) Fractured hydrothermal slabs and white bacterial mats along fractures showing the zones of low-temperature (<100°C) hydrothermal outflow. This area is located near vent 2607 (see Figure 2). (c) Lobate lava flow with numerous collapse structures and lava pillars, and flanked to the E by a sheet flow. Here "fs" is fault scarp, "t" is talus; "b" is bacterial mats associated with low-temperature hydrothermal outflow; "s" is hydrothermal slab; "sf" is sheet flow; "fl" is folded lava flow; "rl" is ropy lava flow; "bl" is brecciated lavas; "lp" is lava pillar; and "c" is collapsed lava flow. One-meter bathymetry contours are shown in Figure 9a as dashed lines.

(~3.8 Gb) from the LUSTRE'96 cruise are available at the Marine Geoscience Data System (MGDS) Web site (http://www.marine-geo.org/link/entry.php?id = KN145-19). The software developed by the University of Girona, including both the Matlab™ functions and the *MosaicViewer* software (compiled for Windows platforms at the present time) are also available on the Web (http://

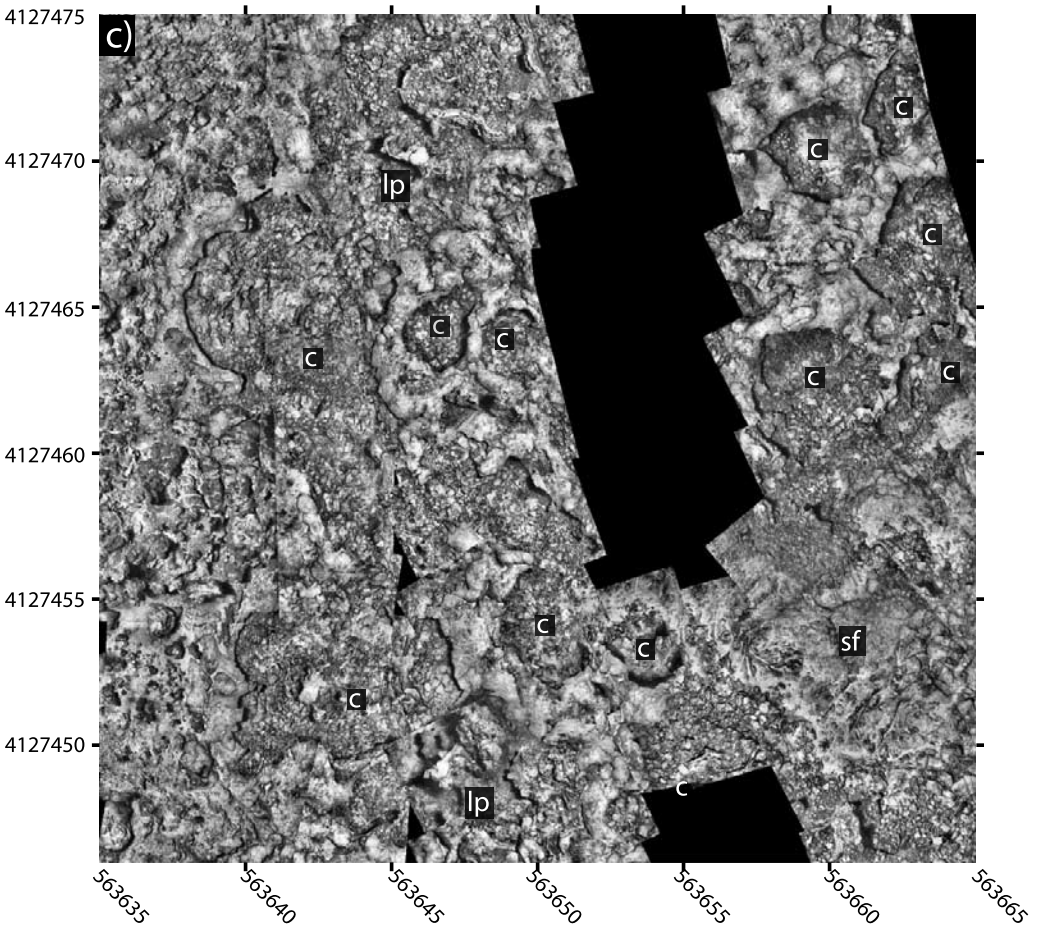

Figure 9. (continued)

eia.udg.es/~rafa/mosaicviewer.html) and are linked to the Lucky Strike data set webpage within the MGDS. The software is provided together with documentation, a small subset of LUSTRE'96 images, an associated navigation file, and a Matlab™ script to be used as an example and guide for use in other data sets. In the near future we will use the site listed above to provide new releases of the software.

4. Data Examples, Discussion, and Perspectives

[28] Selected details of the Lucky Strike mosaic are shown in Figures 9 and 10 and illustrate the utility of visualizing the data using the mosaicing techniques outlined. In particular, mosaics provide both the scale and orientation of seafloor features necessary for geological interpretation, which are not available from the analysis of individual frames from the corresponding image sets. Large fault scarps in the area, extending several km along-axis and with vertical relief of >100 m are clearly visible in the multibeam or side scan sonar data [e.g., *Scheirer et al.*, 2000; *Humphris et al.*, 2002]. Smaller faults at the summit of the central volcano [e.g., *Ondreas et al.*, 1997; *Escartín et al.*, 2005] with scarps of meters to 10s of meters can only be imaged with near-bottom photography. Imaging small scarps is difficult owing to their high relief relative to the observation height of the camera (several 10s of m versus ~10 m). Despite these limitations, mosaics can be used to identify the steeper portions of fault scarps and associated talus (*fs* and *t* in Figure 9a), constrain the overall orientation of tectonic features, and determine their lateral extent. Hydrothermal features (Figure 9b) and volcanic morphology (Figure 9c) are better characterized using mosaics, as the centimeter-to-meter scale of characteristics features is resolved by the seafloor imagery. Zones of diffuse low-temperature flow (<100°C) proximal to the high-temperature vents are often associated with bacterial mats and hydrothermal deposits that are visible as white areas in the greyscale imagery. For exam-

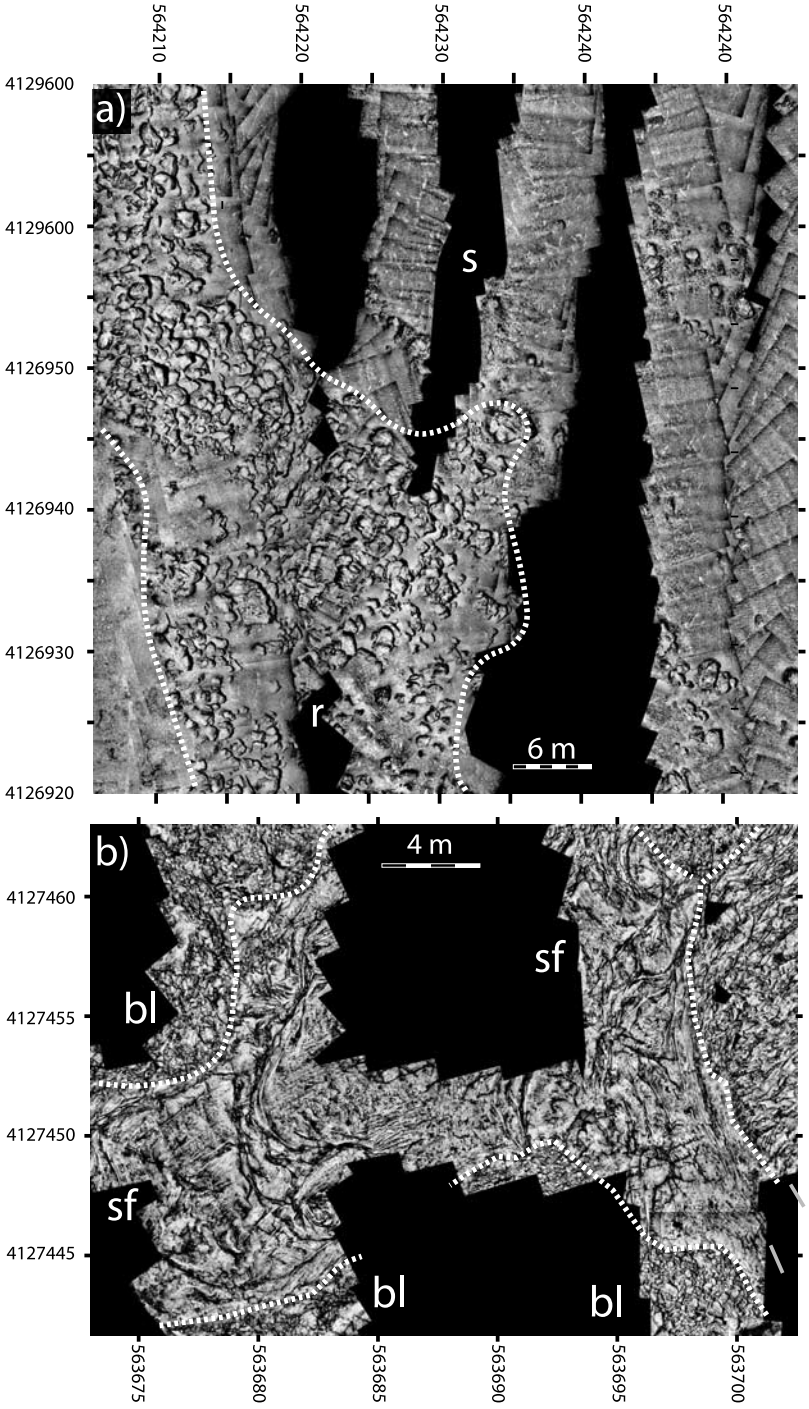

Figure 10. Geometry and nature of contacts as defined by mosaiced and georeferenced images. (a) A large portion of the study area is covered by rubble of volcanic and/or hydrothermal origin, *r*, and sediment, *s*, accumulating preferentially in ponds and often displaying bioturbation marks. The dashed line indicates the boundary between the rubble and the sediment. (b) Lava channel characterized by sheet flows (sf), and a NNW-SSE flow direction of the flow as indicated by the lineations (grey lines). The lava channel is flanked to the East by ropy lavas (rl), with a similar direction of flow (perpendicular to the folding, grey lines), and terminating in brecciated lavas (bl), to the South.

ple, in Figure 9b the zones of interpreted outflow (indicated by "b" in Figure 9b) concentrate along cracks in the hydrothermal slab (indicated by "s" in Figure 9b), and as zones of patchy, more diffuse outflow. Hydrothermal vents rising several meters above the seafloor, however, are difficult to identify in this type of vertical-incidence photographic surveys, as they are poorly imaged and improperly projected when assuming a flat bottom. The central portion of the Lucky Strike hydrothermal field corresponds to a depression (Figure 1b and, 2) that has been infilled by lava. This area is characterized by numerous lava pillars (indicated by "lp" in Figure 9c) and collapsed lava flows (indicated by "c" in Figure 9c) providing evidence of drain back, in addition to the presence of sheeted lava flow channels [e.g., *Ondreas et al.*, 1997; *Humphris et al.*, 2002] (Figure 10).

[29] The geometry of boundaries between different geological units or facies, which provides information on the relative chronology of events and their spatial relationships, can only be properly constrained with georeferenced image mosaics over a large area (Figure 10). Most of the Lucky Strike area is covered by volcanic or hydrothermal rubble, with local sediment ponds (indicated by "r" and "s" in Figure 10a, respectively). Lava ponding of the central Lucky Strike depression has been achieved by a series of flows fed by well-defined lava channels characterized by sheet flows (indicated by "sf" in Figure 10b) and associated folded and ropy lava textures (indicated by "r" in Figure 10b) that locally terminate in brecciated areas (indicated by "bl" in Figure 10b). The direction of flows can also be inferred from both the lineations and the folding of the lava surface (green lines in Figure 10a). Owing to the limited resolution of the mosaics (~15 mm pixels), only larger biological features such zones of bacterial mats and some macro fauna (i.e., fish, *Chimaera*) are visible. The mosaiced images can be digitized to map, quantify, and provide information on volcanic, tectonic, hydrothermal, and biological features and to study the interrelated processes (i.e., volcanic history and provenance of lava flows, relationship between zones of hydrothermal outflow and substrate nature, etc.).

[30] The Lucky Strike photomosaic also provides a first global view of the Lucky Strike hydrothermal field, which can be used as a baseline for temporal studies in the area once additional surveys of the same area are available. This will allow us to quantify changes in the seafloor associated with either the natural evolution of the hydrothermal system (i.e., changes in the distribution of outflow zones or new discharge zones), or with possible tectonic or magmatic events, such as the 2001 seismic crisis recorded by a hydrophone network [*Dziak et al.*, 2004]. This site is also the focus of an ongoing, concerted effort within the Monitoring the Mid-Atlantic Ridge (MoMAR) program (www.momar.org) to develop integrated, long-term monitoring studies of the site, and the implementation of a seafloor observatory as part of the European Seafloor Observatory Network (ESONET). The imagery thus provides a highly detailed characterization of the seafloor that can be used both for the installation of instrumentation (such as cables and sensors) and to manage the site as experiments are carried out in the area.

5. Conclusions

[31] We have generated a complete, georeferenced mosaic of the Lucky Strike vent field at the Mid-Atlantic Ridge, from >20,000 seafloor digital images acquired during the LUSTRE'96 cruise. The imagery, which covers ~20% of the ~1 km^2 hydrothermal field and has a resolution of 15 mm, is the first available complete seafloor image mosaic extending over such a large area. This data set is released through the Marine Geoscience Data System (MGDS, http://www.marine-geo.org/link/entry.php?id = KN145-19) for both scientific purposes and as a resource to plan, implement, and manage experiments within the framework of the MoMAR integrated studies and seafloor observatory efforts in this area. The software developed and used to generate and visualize the mosaic is also released together with the data, so that similar mosaics can be generated from available imagery and associated navigation data by scientists not specialized in image-processing techniques. The software offers both viewing and interpretation capabilities, which can facilitate the visualization and full scientific exploitation of similar image data sets. In addition to quantitative mapping and geological, biological or hydrothermal studies, mosaicing can facilitate the comparison of seafloor imagery for temporal studies, and is potentially an important tool to plan and manage sites for long-term observations and monitoring.

Appendix A: Navigation File

[32] As discussed in the text, mosaic generation requires the user to provide an ASCII navigation

Table A1. Format of Navigation Text File and Parameters Necessary to Create a Mosaic

Image Path	UTMX	UTMY	Altitude	Heading	Pitch	Roll
./Images/ESC.960723_014628.0595.png	564300.6113	4127126.725	7.9424	3.269538	0	0
./Images/ESC.960723_014641.0596.png	564300.6482	4127129.847	8.134399	3.269538	0	0
./Images/ESC.960723_014654.0597.png	564300.684	4127132.969	8.263618	3.263618	0	0
./Images/ESC.960723_014707.0598.png	564300.6842	4127136.426	8.534401	3.254084	0	0
./Images/ESC.960723_014720.0599.png	564300.6554	4127140.17	9.382399	3.250218	0	0
./Images/ESC.960723_014733.0600.png	564300.6272	4127143.914	9.638398	3.250218	0	0

file that includes: image filename path, UTM X and Y coordinates in meters, altitude in meters, heading (0–2π radians), pitch (positive when the front of the vehicle points upwards), and roll (positive when starboard side is down) (shown in Table A1). It should be noted that heading is the clockwise angle with respect to the north (according to the gravity vector of the vehicle).

A1. Matlab™ Functions and Homographies

[33] We provide a Matlab™ function to load the navigation file (*mosaic_generate.m*). This program generates an output structure required by the viewer software to build the mosaic. At this step, only the image file names and the 3-D positions and orientations of the camera are stored. A second function (*mosaic_calc_abs_from_pose.m)* will use this information in order to compute the 2-D position and orientation of each image in the mosaic. Users must provide this function with either the intrinsic camera parameter matrix K [*Bouguet and Perona*, 1998], or its resolution as the length in meters covered by one pixel of the image along one of its axes when the camera is located at 1 m above the ocean floor. The software assumes in later this case that the pixel covers a square surface at the seafloor and computes an approximation of the matrix of intrinsic parameters K from the provided resolution. Moreover, the user can manually set the desired pixel size of the final mosaic (in meters per pixel), based on the resolution of the camera, the altitude of the survey, and the desired final size of the mosaic. If the navigation file refers to the acoustic pinger and not to the camera, the user can also provide the position and orientation of the camera with respect to the pinger.

[34] A 3-D rigid body motion can be expressed by a rotation and translation. In the most general case, rotation ${}^{i}R_{w}$ matrix encodes the three rotation angles between the coordinate system of the camera (when image i was acquired) with respect to an arbitrary reference frame, which we call "world" reference frame hereafter. These three rotation angles are known as roll, pitch, and yaw (or heading) and are the rotations along x, y, and z, respectively. (In this case, the z axis corresponds to the gravity vector of the vehicle when pitch and roll are zero.) Being ${}^{i}R_{w} = R(\theta_x^i) \cdot R(\theta_y^i) \cdot R(\theta_z^i)$, with with

$$R(\theta_x^i) = \begin{bmatrix} 1 & 0 & 0 \\ 0 & \cos(\theta_x^i) & -\sin(\theta_x^i) \\ 0 & \sin(\theta_x^i) & \cos(\theta_x^i) \end{bmatrix},$$

$$R\left(\theta_y^i\right) = \begin{bmatrix} \cos\left(\theta_y^i\right) & 0 & \sin\left(\theta_y^i\right) \\ 0 & 1 & 0 \\ -\sin\left(\theta_y^i\right) & 0 & \cos\left(\theta_y^i\right) \end{bmatrix} \text{ and}$$

$$R(\theta_z^i) = \begin{bmatrix} \cos(\theta_z^i) & -\sin(\theta_z^i) & 0 \\ \sin(\theta_z^i) & \cos(\theta_z^i) & 0 \\ 0 & 0 & 1 \end{bmatrix}.$$

Let K be the matrix that contains the intrinsic camera parameters, defined as:

$$K = \begin{bmatrix} f \cdot k_u & 0 & u_0 \\ 0 & f \cdot k_v & v_0 \\ 0 & 0 & 1 \end{bmatrix} \tag{A1}$$

where f is the focal length of the camera in m, k_u and k_v are the size of every pixel of the camera in m and in the horizontal and vertical directions, respectively, u_0 and v_0 are the coordinates of the "principal point' in pixels, which is the projection of the focal point camera onto the image plane.

[35] And let ${}^{i}H_{w}$ be a planar projective transformation mapping the coordinates of any world point ${}^{w}\tilde{X} = [{}^{w}x, {}^{w}y]^T$ (taking ${}^{w}z = 0$, as we assume a flat ocean floor), to the coordinates of this point in the image plane (in pixels). ${}^{i}H_{w}$ can be expressed as

$${}^{i}H_{w} = K \cdot {}^{i}R_{w} \cdot \begin{bmatrix} 1 & 0 & -{}^{w}t_x \\ 0 & 1 & -{}^{w}t_y \\ 0 & 0 & -{}^{w}t_z \end{bmatrix} \tag{A2}$$

where ${}^{w}t_x$, ${}^{w}t_y$ and ${}^{w}t_z$ are the elements of the translation vector of the camera with respect to the world frame.

[36] The homography ${}^{i}H_w$ can be calculated as shown in equation (A2) for every image *i*. This matrix maps points in the world coordinate frame (in meters) onto the image frame (in pixels). In the same way, $({}^{i}H_w)^{-1} = {}^{w}H_i$ maps images points to a 2-D world frame (as we set ${}^{w}z = 0$) which is the mosaic frame. The whole mosaic frame is then scaled and cropped in order to have the desired resolution and size.

[37] Finally, when all the 2-D homographies are computed and stored in the Matlab™ structure, this one can be saved with the function *gmml_save.m* that generates an output file (GMML metalanguage, see below).

[38] Additional Matlab™ functions to visualize the coverage and position of individual images of the mosaic and to calculate the position and orientation of the camera using the navigation and attitude of the vehicle and the position of sensors (acoustic transponder, altimeter, gyro) are also provided. All functions contain the required help information. The software is released with a test data set of images and corresponding navigation from the Lucky Strike area and a script for its processing and visualization.

A2. GMML File

[39] The General Mosaic Markup Language (GMML), a format defined in a XML format, has been devised at the University of Girona to encode information to build the photomosaic. GMML files, which are generated by the Matlab™ *gmml_save.m* function, is headed by an initial (''INIT'') field containing the information relative to the mosaic; the UTM coordinates of the mosaic origin (top left corner), the size of the complete mosaic, and the pixel resolution in m. The mosaic definition is followed by nodes containing the information relative to each of the images used to build the photo-mosaic. The ''NODES'' field includes the filename of the image, the homography, and the position of the camera, among other information. Each node contains a field ''EDGES'' that tracks previous images that overlap with it (i.e., nodes corresponding to images with a lower index).

A3. MosaicViewer: Mosaic Generation, Visualization, and Exploitation

[40] The *MosaicViewer* software is released as an executable for PC running Windows XP and Linux operating systems; executables for other platforms and operating systems (Mac OSX, Windows Vista) will be provided in the future. A first function of the viewer is the construction of mosaics using the GMML files and the corresponding digital photos. This software generates a set of tiles at full resolution for the whole mosaic area (>300 files in the case of the LUSTRE'96 mosaics). Additional tiles of progressively lower resolution are generated to create a multiresolution image pyramid that is accessed by the viewer. This scheme allows the visualization of very large image mosaics (e.g., 78,212 by 92,540 pixels for the full LUSTRE'96 mosaic), with fast and efficient zooming and panning capabilities. The software has a simple interface to visualize, import and export data; the list below provides some of the main functions available, which are described in detail in documentation released with the software:

[41] 1. Zooming and panning.

[42] 2. Import and export of UTM x and y coordinates, with simple color and symbol attributes. Toggling on and off the display of loaded files.

[43] 3. Import and export of lines or polygon UTM x and y coordinates with color attributes. Toggling on and off the display of loaded files.

[44] 4. Export of images of selected areas (window, UTM-defined box or mouse-selected area) and an associated metadata file (TFW format, including the coordinates of the NW corner of the image and the pixel size in m along the x and y directions).

[45] 5. Visualization of multiple mosaics (windows) and possibility of synchronizing their location and scales.

[46] 6. When a GMML mosaic definition and imagery are loaded together with the multiresolution mosaic image, which allows the detection of positions and intersections of source images, and finds source images contained in selected regions.

Acknowledgments

[47] This work has been supported by the EU Marie Curie RTNs MOMARNet (OD, RG, JE, LN, JF, NG) and FREESUBNet (RG, NG, XC), the Spanish Ministry of Science and Innovation (grant CTM2007–64751; RG, JE), CNRS and ANR (grant ANR NT05–3_42212, JE), ICREA (LN), and by the Generalitat de Catalunya (JE, RG). JF has been funded by MICINN under FPI grant BES-2006-12733 and NG has been supported by MICINN under the ''Ramon y Cajal'' program. The images used in the mosaicing were acquired during the LUSTRE'96 cruise on board R/V *Knorr* with

funding from NSF OCE-9505579 DJF and SEH and OCE-0074846 to SEH. We thank the Captain and crew of *Knorr* and the ROV *Jason* technical team and the shipboard scientific party for their assistance in collecting these data and S. Gegg and J. Howland (WHOI) for providing technical information on the survey and instrumentation. This is IPGP contribution 2424.

References

Bachmayer, R., et al. (1998), Oceanographic exploration of hydrothermal vent sites on the Mid-Atlantic Ridge at 37 N 32 W using remotely operated vehicles, *Mar. Technol. Soc. J.*, *32*, 37–47.

Ballard, R., L. Stager, D. Master, D. Yoerger, D. Mindell, L. Whitcomb, H. Singh, and D. Piechota (2002), Iron age shipwrecks in deep water off Ashkelon, Israel, *Am. Inst. Archaeol.*, *106*, 151–168, doi:10.2307/4126241.

Bay, H., T. Tuytelaars, and L. J. V. Gool (2006), SURF: Speeded Up Robust Features, in *Computer Vision: Ninth European Conference on Computer Vision*, edited by A. Leonardis, H. Bischof, and A. Pinz, pp. 404–417, Springer, Berlin.

Beaudet, P. (1978), Rotationally invariant image operators, *Proc. Int. Jt. Conf. Pattern Recognit.*, *4*, 579–583.

Bouguet, J.-Y., and P. Perona (1998), 3D photography on your desk, in *Computer Vision: Fifth European Conference on Computer Vision*, edited by H. Burkhardt and B. Neumann, pp. 43–50, Springer, Berlin. (Available at http://www.vision.caltech.edu/bouguetj/calib_doc/)

Bowen, A., D. Fornari, J. Howland, and B. Walden (1993), The Woods Hole Oceanographic Institution's remotely operated and towed vehicle facilities for deep ocean research: Information and specifications, version 1.0, Woods Hole Oceanogr. Inst., Woods Hole, Mass.

Brown, M., and D. G. Lowe (2003), Recognising panoramas, in *Computer Vision: Third European Conference on Computer* Vision, edited by J. L. Crowley et al., pp. 1218–1225, Springer, Berlin.

Charlou, J. J., J. P. Donval, E. Douville, P. Jean Baptiste, J. Radford-Knoery, Y. Fouquet, A. Dapoigny, and M. Stievenard (2000), Compared geochemical signatures and the evolution of Menez Gwen (37°50′N) and Lucky Strike (37°17′N) hydrothermal fluids, south of the Azores Triple Junction on the Mid-Atlantic Ridge, *Chem. Geol.*, *171*, 49–75, doi:10.1016/S0009-2541(00)00244-8.

Dziak, R. P., D. K. Smith, D. R. Bohnenstiehl, C. G. Fox, D. Desbruyères, H. Matsumoto, M. Tolstoy, and D. J. Fornari (2004), Evidence of a recent magma dike intrusion at the slow spreading Lucky Strike segment, Mid-Atlantic Ridge, *J. Geophys. Res.*, *109*, B12102, doi:10.1029/2004JB003141.

Escartín, J., S. Soule, D. J. Fornari, M. Cannat, and S. Humphris (2005), Tectonic interaction along the Lucky Strike rift valley floor: Controls on hydrothermal distribution, *Eos Trans. AGU*, *86*(52), Fall Meet. Suppl., Abstract OS33A–1463.

Eustice, R., H. Singh, J. Leonard, and M. R. Walter (2006), Visually Mapping the RMS Titanic: Conservative Covariance Estimates for SLAM Information Filters, *Int. J. Robot. Res.*, *25*, 1223–1242, doi:10.1177/0278364906072512.

Ferrer, J., A. Elibol, O. Delaunoy, N. Gracias, and R. Garcia (2007), Large-area photo-mosaics using global alignment and navigation data, paper presented at Oceans Conference, Mar. Technol. Soc., Vancouver, British Columbia, Canada.

Fischler, M., and R. Bolles (1981), Random sample consensus: A paradigm for model fitting with applications to image analysis and automated cartography, *Commun. Assoc. Comput. Mach.*, *24*(6), 381–395.

Fouquet, Y., J. L. Charlou, I. Costa, J. P. Donval, J. Radford-Knoery, H. Pellé, H. Ondréas, N. Lourenço, M. Ségonzac, and M. K. Tivey (1994), A detailed study of the Lucky Strike hydrothermal site and discovery of a new hydrothermal site: Menez Gwen; Preliminary results of the DIVAI Cruise (5–29 May, 1994), *InterRidge News*, *3*, 14–17.

Garcia, R., X. Cufí, and V. Ila (2003), Recovering camera motion in a sequence of underwater images through mosaicking, *Lect. Notes Comput. Sci.*, *2652*, 255–262.

German, C., D. Yoerger, T. Shank, M. Jakuba, A. Bradley, A. Billings, R. Catanach, A. Dester, K. Nakamura, C. Langmuir, L. Parson, and A. Koschinsky (2006), Hydrothermal exploration by AUV: ABE in the Lau Basin and South Atlantic, *Eos Trans. AGU*, *87*(52), Fall Meet. Suppl., Abstract OS33A–1681.

Harris, C. G., and M. J. Stephens (1988), A combined corner and edge detector, paper presented at Alvey Vision Conference, Manchester Univ., Manchester, U.K.

Humphris, S. E., D. J. Fornari, D. S. Scheirer, C. R. German, and L. M. Parson (2002), Geotectonic setting of hydrothermal activity on the summit of Lucky Strike seamount (37°17′N, Mid-Atlantic Ridge), *Geochem. Geophys. Geosyst.*, *3*(8), 1049, doi:10.1029/2001GC000284.

Langmuir, C., et al. (1997), Hydrothermal vents near a mantle hot spot: The Lucky Strike vent field at 37°N on the Mid-Atlantic Ridge, Earth Planet, *Sci. Lett.*, *148*, 69–91, doi:10.1016/S0012-821X(97)00027-7.

Lindeberg, T. (1998), Feature detection with automatic scale selection, *Tech. Rep. 30*, Comput. Vision and Active Perception Lab., Stockholm, Sweden.

Lowe, D. (2004), Distinctive image features from scale-invariant keypoints, *Int. J. Comput. Vis.*, *60*(2), 91–110, doi:10.1023/B:VISI.0000029664.99615.94.

Marzotto, R., A. Fusiello, and V. Murino (2004), High resolution video mosaicing with global alignment, paper presented at Conference on Computer Vision and Pattern Recognition, IEEE, Washington, D. C.

Mikolajczyk, K., T. Tuytelaars, C. Schmid, A. Zisserman, J. Matas, F. Schaffalitzky, T. Kadir, and L. Van Gool (2005), A comparison of affine region detectors, *Int. J. Comput. Vis.*, *65*, 43–72, doi:10.1007/s11263-005-3848-x.

Negahdaripour, S., R. Prados, and R. Garcia (2005), Planar homography: Accuracy analysis and applications, paper presented at International Conference on Image Processing, IEEE, New York.

Ondreas, H., Y. Fouquet, M. Voisset, and J. Radford-Knoery (1997), Detailed study of three contiguous segments of the Mid-Atlantic Ridge, South of the Azores (37°N to 38°30′N), using acoustic imaging coupled with submersible observations, *Mar. Geophys. Res.*, *19*, 231–255, doi:10.1023/A:1004230708943.

Ondreas, H., M. Cannat, Y. Fouquet, A. Normand, P. M. Sarradin, and J. Sarrazin (2008), Recent volcanic events and the distribution of hydrothermal venting at the Lucky Strike hydrothermal field, Mid-Atlantic Ridge, *Geochem. Geophys. Geosyst.*, doi:10.1029/2008GC002171, in press.

Rzhanov, Y., L. A. Mayer, D. Fornari, T. M. Shank, S. Humphris, D. Scheirer, J. Kinsey, and L. L. Whitcombe (2003), High-resolution photo-mosaicing of the Rosebud hydrothermal vent site and surrounding lava flows, Galapagos Rift 86W: Techniques and interpretation, *Eos Trans. AGU*, *84*(46), Fall Meet. Suppl., Abstract OS32A–0231.

Salamin, E. (1979), Application of quaternions to computation with rotations, technical report, Stanford Univ., Stanford, Calif.

Sawhney, H., S. Hsu, and R. Kumar (1998), Robust video mosaicing through topology inference and local to global alignment, in *Computer Vision: Fifth European Conference on Computer Vision*, edited by H. Burkhardt and B. Neumann, pp. 103–119, Springer, Berlin.

Scheirer, D. S., D. J. Fornari, S. E. Humphris, and S. Lerner (2000), High-resolution seafloor mapping using the DSL-120 sonar system: Quantitative assessment of sidescan and phase-bathymetry data from the Lucky Strike segment of the Mid-Atlantic Ridge, *Mar. Geophys. Res.*, *21*, 121–142, doi:10.1023/A:1004701429848.

Singh, S. C., W. C. Crawford, H. Carton, T. Seher, V. Combier, M. Cannat, J. P. Canales, D. Düsünur, J. Escartín, and J. Miranda (2006), Discovery of a magma chamber and faults beneath a Mid-Atlantic Ridge hydrothermal field, *Nature*, *442*, 1029–1032, doi:10.1038/nature05105.

Singh, H., C. Roman, O. Pizarro, R. Eustice, and A. Can (2007), Towards high-resolution imaging from underwater vehicles, *Int. J. Robot. Res.*, *26*, 55–74, doi:10.1177/0278364907074473.

Soule, S. A., D. J. Fornari, M. R. Perfit, M. A. Tivey, W. I. Ridley, and H. Schouten (2005), Channelized lava flows at the East Pacific Rise crest 9°-10°N: The importance of off-axis lava transport in developing the architecture of young oceanic crust, *Geochem. Geophys. Geosyst.*, *6*, Q08005, doi:10.1029/2005GC000912.

Triggs, B. (1998), Autocalibration from planar scenes, in *Computer Vision: Fifth European Conference on Computer Vision*, edited by H. Burkhardt and B. Neumann, pp. 89–105, Springer, Berlin.

Triggs, B., P. McLauchlan, R. Hartley, and A. Fitzgibbon (2000), Bundle adjustment - A modern synthesis, in *Vision Algorithms: Theory and Practice*, edited by W. Triggs, A. Zisserman, and R. Szeliski, pp. 298–375, Springer, New York.

Vincent, E., and R. Laganière (2001), Detecting planar homographies in an image pair, paper presented at Symposium on Image and Signal Processing and Analysis, IEEE, Pula, Croatia.

Von Damm, K. L., A. M. Bray, L. G. Buttermore, and S. E. Oosting (1998), The geochemical controls on vent fluids from the Lucky Strike vent field, Mid-Atlantic Ridge, *Earth Planet Sci. Lett.*, *160*, 521–536, doi:10.1016/S0012-821X(98)00108-3.

Yoerger, D., M. Jakuba, A. M. Bradley, and B. Bingham (2007), Techniques for deep sea near bottom survey using an autonomous underwater vehicle, *Int. J. Robot. Res.*, *26*, 41–54, doi:10.1177/0278364907073773.

Zitová, B., and J. Flusser (2003), Image registration methods: A survey, *Image Vis. Comput.*, *21*, 977–1000, doi:10.1016/S0262-8856 (03)00137-9.

Zuiderveld, K. (1994), *Graphics Gems IV*, edited by P. S. Heckbert, pp. 474–485, Academic, Boston, Mass.